Assessment of Active Dopants and p–n Junction Abruptness Using In Situ Biased 4D-STEM

Bruno César da Silva, Zahra Sadre Momtaz, Eva Monroy, Hanako Okuno, Jean-Luc Rouviere, David Cooper, Martien Ilse den Hertog

Assessment of active dopants and *p-n* junction abruptness using in-situ biased 4D-STEM

Bruno César da Silva*[1], Zahra Sadre Momtaz[1], Eva Monroy[2], Hanako Okuno[3], Jean-Luc Rouviere[3], David Cooper[4] and Martien Ilse Den Hertog[1]

[1]*Univ. Grenoble Alpes, CNRS-Institut Néel, F-38000 Grenoble, France*

[2]*Univ. Grenoble Alpes, CEA, Grenoble INP, IRIG, PHELIQS, F-38000 Grenoble, France*

[3]*Univ. Grenoble Alpes, CEA, IRIG, MEM, LEMMA, F-38000 Grenoble, France*

[4]*Univ. Grenoble Alpes, CEA-LETI, F-38000 Grenoble, France*

bruno-cesar.da-silva@neel.cnrs.fr

Abstract

A key issue in the development of high-performance semiconductor devices is the ability to properly measure active dopants at the nanometer scale. In a *p-n* junction, the abruptness of the dopant profile around the metallurgical junction directly influences the electric field. Here, a contacted nominally-symmetric and highly doped ($N_A = N_D = 9 \times 10^{18}\ cm^{-3}$) silicon *p-n* specimen is studied through in-situ biased four dimensional scanning transmission electron microscopy (4D-STEM). Measurements of electric field, built-in voltage, depletion region width and charge density are combined with analytical equations and finite-element simulations in order to evaluate the quality of the junction interface. It is shown that all the junction parameters measured are compatible with a linearly graded junction. This hypothesis is also consistent with the evolution of the electric field with bias, as well as off-axis electron holography data. These results demonstrate that in-situ biased 4D-STEM can allow a better understanding of the electrostatics of semiconductor p-n junctions with nm-scale resolution.

Keywords: In-situ biasing transmission electron microscopy, four dimensional scanning transmission electron microscopy, silicon *p-n*, active dopants, built-in electric field, space charge region, linearly graded p-n junction

The reduction in size of semiconductor devices leads to improvements in both performance and cost. However, in nanodevices difficulties may arise in controlling the electrically active dopants and their effect on the electric field.[1–4] Therefore, quantitative methods to measure the electrically active dopant density and profile with nm-scale resolution and high sensitivity are required for the successful engineering of device performance.

Profiling the dopant concentration in a semiconductor can be done by secondary ion mass spectrometry (SIMS)[5] or atom probe tomography (APT).[6] However, these techniques are destructive and only sensitive to the chemical nature of dopants, and not to their electrical activity. Another view is given by electrical transport measurements, such as Hall effect and capacitance-voltage (CV) measurements.[3,7,8] Standard Hall effect can measure the free carrier density and mobility, but not the dopant profile. In contrast, CV characterization offers a good approach to measure the depletion region width and the profile of active dopants. However, it is limited in "depth", and it provides an averaged view of the *n* and *p* regions, unless the junction is extremely asymmetric.[3,9,10] The electrochemical version of CV measurements (ECV) is not 'depth limited', but it is destructive.

Techniques based on transmission electron microscopy (TEM) can provide access to the profile of active dopants[11], defects or polarization fields[12], with nanometer spatial resolution. Off-axis electron holography for example has successfully been used to measure the built-in potential and estimate the active dopant concentration with a spatial resolution down to 1 nm.[13–16] This technique can image built-in potential across lamella samples prepared from bulk *p-n* junctions or nanomaterials such as nanowires[15,17], and can be used combined with in-situ biasing[13,17]. Holography requires a vacuum region close to the sample for the reference wave, and this can be difficult to combine with a reliable electrical contact in the case of nanomaterials[18]. Approaches based on scanning (transmission) electron microscopy (SEM or STEM), such as electron beam induced current (EBIC)[19,20] and differential phase contrast (DPC)[21,22], are also able to study the electrostatics of a *p-n* junction. Unfortunately,

quantification from DPC with a segmented detector is not straightforward and depends on the so called hard shift of the disk to provide reliable results[23], while in EBIC the electric field is mapped qualitatively and is convoluted with the carrier diffusion length. In both cases, quantitative information can be challenging or impossible to extract.

Advances in detector technology have led to the development of four-dimensional (4D) STEM, where the conventional segmented annular dark field detectors are replaced by high-speed pixelated devices, allowing the recording of the convergent beam electron diffraction (CBED) pattern at each scan point of the electron beam, resulting in an electron diffraction map: a 4D data set (two dimensions for the scanning directions and two dimensions in the diffraction patterns). In particular, the implementation of momentum-resolved 4D-STEM has allowed to measure internal electric fields with ultrahigh spatial resolution.[24–26] This includes long-range built-in electric fields at *p-n* junctions. Beyer et al.[26], working in high-resolution STEM conditions with the crystal on-axis and properly estimating the active sample thickness, have demonstrated a reasonable quantification of built-in electric field in a GaAs *p-n* junction, but no in-situ biasing was used. In addition, the low signal-to-noise ratio (SNR) hindered the extraction of the charge density from the derivative of the electric field. In-situ biasing can be a useful tool to evaluate the *p-n* junction interface quality, by following the dependence of the electric field with the external voltage. A similar strategy, but measuring the capacitance instead of the electric field, is used in CV measurements.[3] Recently, we have demonstrated that nanobeam STEM mode can provide reliable electric field maps in a *p-n* junction even with low electron dose.[27]

In the present study, we report in-situ biased 4D-STEM experiments, using a high-speed pixelated direct electron detector with Medipix3 technology, performed on a Si *p-n* junction with electrical contacts. The high speed acquisition enables to acquire large field of view maps at different biases without sample drift. This approach leads to reliable measurements of the charge density, electric field and electrostatic potential as a function of bias, with a large field of view. The interpretation of the results does not require advanced modeling of the junction, and the measurement does not require the presence of a vacuum region close to the specimen. Measurements are compared to finite element simulations, as well as SIMS and electron holography measurements performed in the same wafer.

The sample under study is a symmetrically doped silicon *p-n* junction grown by reduced-pressure chemical vapor deposition. Dopants were phosphorus for the *n*-type region and boron for the *p*-type segment, both at a concentration of $9 \times 10^{18}\ cm^{-3}$. The lamella specimen was mounted in a Protochips Aduro 500 system and prepared using a FEI Strata dual beam focused ion beam (FIB) tool. The specimen was welded by FIB-assisted metal (W) deposition across a biasing chip, and isolation cuts were made so that bias is applied across the *p-n* junction. The specimen was prepared using optimized protocols to reduce gallium implantation.[28] The crystalline thickness of the sample was measured using the CBED patterns acquired in two beam condition.[29] This method can provide a measurement of the crystalline sample thickness with an accuracy of ± 5 nm.[28,29] In addition, the dead layer thickness was extracted using off-axis electron holography by measuring the step in phase of samples prepared from the same wafer by FIB with different specimen thickness.[19] The lamella under study presented a total thickness $t_{crystal} = (350 \pm 10)\ nm$, with an electrically inactive region thickness $t_{dead} = (60 \pm 15)$ nm at the surfaces.[19]

4D-STEM was performed in a FEI Titan Ultimate aberration-corrected (S)TEM microscope operated at 200 kV and equipped with a fast pixelated (256 × 256 pixels) Medipix3-based Merlin camera. Measurements were performed in nanobeam STEM mode, using a nominal semiconvergence angle of 1.09 mrad and a camera length of 2.3 m. With these settings, there are no overlapping disks in the CBED patterns, and the pixelated detector records the transmitted beam. The probe diameter was estimated from a TEM image (Figure S1a); its full width at half maximum is about 3.6 nm. In reciprocal space, the angular resolution (the pixel size in the pixelated detector) was 11.0 µrad. Electron diffraction patterns of 178 × 105 pixels were acquired in the single-pixel mode of the Merlin detector, with a threshold t_0 = 80 kV. A representative diffraction pattern is shown in Figure S1b. Experiments were performed using a beam current of 100 pA, a step size of 5 nm and a dwell time for each diffraction pattern of 5 ms. The sample was tilted off-axis around the growth direction to minimize the diffraction contrast while keeping the *p-n* junction perpendicular to the direction of the electron beam. It is well known that the presence of dynamical diffraction leads to measurements of the field that are incorrect, therefore a live DPC on a 4-quadrant DPC detector was used to establish a crystal orientation with reduced diffraction contrast.[22] Biased measurements were carried out by recording the 4D data set while bias was applied on the sample using an external Keithley source. Figure 1 shows a schematic description of the momentum-resolved 4D-STEM experiments on the Si lamella containing a *p-n* junction. Reverse (forward) bias is used to increase (decrease) the electric field at the junction. Data analysis of the 4D data sets was carried out with python scripts using basic open-source libraries (e.g. HyperSpy).[30] The electric field was estimated from the deflection of the electron beam when passing through

the region with electric field, using a region without field as a reference. The deflection is extracted from the measurement of the center-of-mass of the transmitted disk in the acquired diffraction patterns. The electron beam deflection is converted into electric field using[22]

$$E_{\perp} = -\frac{\gamma m_e^* v_0^2}{qt} \quad (1)$$

where q is the elementary charge, γ is the electron beam deflection, m_e^* the relativistic mass of the electron, v_0 the relativistic electron velocity, and t the active sample thickness. The active sample thickness is obtained by $t = t_{crystal} - t_{dead}$. In the setting used, the interaction of the electron beam with the sample resulted in a hard shift of the transmitted beam, as previously reported,[27] justifying the use of eq. 1 to properly estimate the electric field. The main uncertainty in the measurement of the electric field is due to the detection process (including Poisson noise), as described in Supporting Information SI1b.

The *p-n* junction was previously characterized by SIMS, electron holography, EBIC and 4D-STEM with precession diffraction.[14,19,22,31] The SIMS profile, provided as Supporting Information SI2, confirms *n* and *p* dopant concentrations $N_A = N_D = 9 \times 10^{18} cm^{-3}$ in the bulk areas, and shows that the junction may not present a sharp interface, but it is rather a *p-i-n* structure. The depth resolution of SIMS is degraded when increasing the penetration depth in the sample due to self-implantation and roughening. Therefore, we can only provide an upper limit of the intermediate region length, which is about 200 nm.

Figure 2a shows the electric field maps measured by momentum-resolved 4D-STEM at different bias. Under forward bias, both the electric field and the depletion region width decrease, while under reverse bias, the electric field and the depletion region width increase. Figure 2b shows the variation of the electric field profile across the junction. A noise level of $0.03\ MV cm^{-1}$ was estimated by measuring the standard deviation ($1\sigma_E$) of the electric field maps in an area of 100 nm × 70 nm where the field was nominally zero. At zero bias, a depletion region width $W_d = (73 \pm 11)\ nm$ and a maximum electric field $E_{max} = (0.176 \pm 0.03)\ MV cm^{-1}$ were found. The analysis of the uncertainty of the depletion region width if given in SI1c. A table with the E_{max} and W_d extracted as a function of bias is shown in Supporting Information SI3.

The built-in potential, V_{bi}, can be retrieved by integrating the electric field shown in Figure 2b. At zero bias, we estimate $V_{bi} = (0.88 \pm 0.06)\ V$. These results were compared to electron holography measurements performed in the same wafer (Supporting Information SI4), which lead to $V_{bi} = (0.86 \pm 0.05)\ V$ and $E_{max} = (0.175 \pm 0.02)\ MV cm^{-1}$,[14,19] in good agreement with 4D-STEM results. These values were obtained considering the 60 nm dead layer previously measured for the same wafer.[19]

In Supporting Information SI5, we recall the abrupt and linearly graded junction approximations. Both the 4D-STEM and electron holography results cannot be explained by the abrupt junction approximation, since the dopant concentration $N_A = N_D = 9 \times 10^{18} cm^{-3}$ obtained by SIMS (SI2) should lead to $W_d = 12\ nm$, $V_{bi} = 1.06\ V$ and $E_{max} = 0.859\ MV cm^{-1}$, as summarized in Table 1. Keeping to the abrupt model, the experimental results would rather correspond to a junction with a doping level in the range of $N_A = N_D = (2.8 - 4.5) \times 10^{17}\ cm^{-3}$ (see Table 1). The huge difference between nominal and experimental results can be explained by the presence of the intermediate region between the *p* and *n* layers. Looking at the SIMS profiles, a ≈ 73 nm wide depletion should be fully contained in the intermediate region, so that it could be modeled as a linearly graded junction. The experimental results can be reproduced assuming a linearly graded junction with a dopant variation per unit of length $\alpha = 1.5 \times 10^{23}\ cm^{-4}$ (see Table 1). However, using this model, the value of V_{bi} remains on the higher part of the error bar of the experimental results. With this value of α, and keeping in mind the doping levels in the bulk *n* and *p* regions ($N_A = N_D = 9 \times 10^{18} cm^{-3}$), the width of the linearly graded region should be $W_G = (N_A + N_D)/\alpha = 1.1\ \mu m$, which is inconsistent with SIMS measurements. Therefore, we assume that the junction is almost linearly graded in an intermediate region that extends over 200 nm, and the doping level increases rapidly outside this region.

As additional information, the density of ionized dopants can be extracted from the derivative of the electric field shown in Figure 2a, using Poisson's equation. The result is shown in Figure 3a. The space charge region is clearly visible with a slight asymmetry between the *n* and *p* side, as observed in the SIMS data (Figure S2). In Figure 3b, the charge density profiles were averaged along the entire map, in order to reduce noise. At zero bias, we have found a maximum charge density $N_{Dmax} = (4.0 \pm 0.7) \times 10^{17}\ cm^{-3}$ on the *n* side and $N_{Amax} = -(3.1 \pm 0.7) \times 10^{17}\ cm^{-3}$ on the *p* side. These values are consistent with a built-in voltage $V_{bi} = 0.89\ V$, and confirm that the reduced electric field extracted from 4D-STEM is due to the small amount of active dopants, more

than one order of magnitude smaller than the nominal value. This cannot be explained by partial ionization, looking at the low ionization energy of boron and phosphorus in silicon.[32] We also rule out a screening effect due to the electron beam, since our experiments were performed in the low injection regime, as shown in Supporting Information SI6. In summary, all the experimental results suggest that the reduced electric field and charge density are indeed due to the graded nature of the junction.

We have verified that the linearly graded model is compatible with the variation of the electric field with bias. In a linearly graded junction, following eq. S18, $|E_{max}| \propto (V_{bi} - V)^{\frac{2}{3}}$. Figure 4 shows the variation of $|E_{max}|$ with bias compared with the theoretical values for different impurity grandients α in the range of $4 \times 10^{22}\ cm^{-4}$ to $4 \times 10^{23}\ cm^{-4}$. A good agreement is found for $\alpha = 1.5 \times 10^{23}\ cm^{-4}$, consistent with the above-described results.

The analytic equations in SI5 assume that the space charge region is fully depleted. As a consequence, the built-in potential is determined by the doping level at the edges of the depletion region ($x = \pm W_d/2$). Assuming $\alpha = 1.5 \times 10^{23}\ cm^{-4}$, we obtain $N(x = \pm W_d/2) = 5.9 \times 10^{17}\ cm^{-3}$, which leads to $V_{bi} = 0.918\ V$, as presented in Table 1. Both this charge density and the built-in voltage are higher than the estimations from 4D-STEM. To understand this difference, we have to keep in mind that the charge distribution at room temperature is more complex than the depletion approximation. A tail of the electron and hole distribution penetrates the space charge region, whose limits are therefore not abrupt. In a linearly graded junction, this means that the maximum net charge density does not occur at the edges of the depletion region, but it is slightly shifted towards the junction interface. This is experimentally observed in Figure 3b, where the distance between the locations of maximum charge density is clearly smaller than W_d. As the charge density does not attain the maximum value of dopant concentration, located at ($x = \pm W_d/2$), this leads to a reduction of the built-in voltage.

To incorporate these thermal effects in our model, 1D simulations of the silicon *p-n* junction have been performed solving the Poisson equation numerically using the nextnano3 software. Figure 5a proposes a dopant profile (blue curve) that consists of a linearly graded junction with $\alpha = 1.5 \times 10^{23}\ cm^{-4}$, which extends over $W_G = 200\ nm$ (distance chosen to be coherent with the SIMS profile (SI2)). Outside this intermediate region, the dopant concentrations rapidly reach the bulk values: $N_A = N_D = 9 \times 10^{18}\ cm^{-3}$. Figures 5b, c present the comparison between simulated and measured electric field (absolute value) and charge density, respectively, at zero bias. The overall electrostatic parameters of the junction (electric field, depletion region and maximum charge density) are well reproduced with our extremely simplified model. A slightly better fit is obtained with $\alpha = 1.8 \times 10^{23}\ cm^{-4}$, instead of $\alpha = 1.5 \times 10^{23}\ cm^{-4}$. The fact that the two charge density maxima in Figure 5c are closer in the experimental curve than in the simulation is due to the fact that the real dopant profile is not perfectly linear, but slightly superlinear.

It is worth highlighting that the 4D-STEM provides a direct measurement of the electric field (Figure 2b) and charge distribution (Figure 3b) in the space charge region, without any assumption in terms of doping profile, unlike other techniques like CV measurements[3] or EBIC.[33] A challenge for quantitatively evaluating the electric field by 4D-STEM is the unknown value of the electrically inactive sample thickness[13], which is often speculated to be at the origin of measuring a lower built-in potential than expected supposing an abrupt *p-n* junction in electron holography.[13] However, the error associated with the surface dead layer can be identified and corrected by measuring the electron beam deflection or phase shift as a function of the sample thickness, as demonstrated both for 4D-STEM[26] and electron holography.[13,14,34] Here, we have demonstrated that the measurement of an electric field lower than the nominal value is not necessarily an artifact. It can originate from a nonideal doping profile. Careful 4D-STEM measurements incorporating the dead layer thickness correction and in-situ biasing can provide valuable information about the doping profile. In particular, it is possible to determine the degree of ideality of the junction, detecting phenomena like dopant segregation or interdiffusion.

In summary, we have combined in-situ biasing and momentum-resolved 4D-STEM measurements of a symmetric silicon *p-n* junction, previously analyzed by SIMS and off-axis electron holography. We have obtained a maximum electric field $E_{max} = (0.176 \pm 0.03)\ MV cm^{-1}$, in agreement with electron holography results. The charge density distribution in the space charge region was directly extracted from the 4D-STEM measurement of the electric field. The comparison of the measured values with analytical equations, as well as finite element simulations, demonstrates that the dopant density profiles do not drop abruptly at the junction. Instead, this sample can be reasonably well modeled as a linearly graded *p-n* junction with an impurity gradient in the range of $\alpha = (1.5 \pm 0.7) \times 10^{23}\ cm^{-4}$.

The development of more efficient semiconductor devices, currently reaching the nanoscale, demands tools able to provide fast feedback for further device optimization. Our results show that in-situ biased 4D-STEM is a suitable approach to study the interface quality of *p-n* junctions, enabling the measurement of crucial electrical properties of such devices.

Supplementary Material

The Supporting Information is available free of charge at https://pubs.acs.org/doi/10.1021/acs.nanolett.2c03684 .
4D-STEM raw data example, analysis of the uncertainty of the electric field and depletion region width measurements, SIMS and off-axis electron holography measurements performed in the same wafer, recall of the abrupt and linearly graded p−n junction approximations, and calculations of the validity of the weak injection condition using the parameters used in these experiments (PDF)

Acknowledgements

Martien I. den-Hertog, B. C. da S., Z. S. M., H. O., E. M. and J. L. R. thank the European Union's Horizon 2020 research and innovation programme under the European Research Council (ERC) Grant agreement N° 758385 (e-See). These experiments have been performed at the Nanocharacterisation platform (PFNC) based at Minatec, Grenoble.

Data Availability Statement

The data that support the findings of this study are available from the corresponding authors upon reasonable request.

Notes

The authors declare no competing financial interest.

References

(1) Sze, S. M.; Ng, K. K. *Physics of Semiconductor Devices*, 3. ed.; Wiley-Interscience: Hoboken, NJ, 2007.
(2) Sze, S. M.; Gibbons, G. AVALANCHE BREAKDOWN VOLTAGES OF ABRUPT AND LINEARLY GRADED *P-n* JUNCTIONS IN Ge, Si, GaAs, AND GaP. *Appl. Phys. Lett.* **1966**, *8* (5), 111–113. https://doi.org/10.1063/1.1754511.
(3) Dmitriev, V. A.; Irvine, K. G.; Carter, C. H.; Kuznetsov, N. I.; Kalinina, E. V. Electric Breakdown in GaN *P-n* Junctions. *Appl. Phys. Lett.* **1996**, *68* (2), 229–231. https://doi.org/10.1063/1.116469.
(4) Kim, W.; Güniat, L.; Fontcuberta i Morral, A.; Piazza, V. Doping Challenges and Pathways to Industrial Scalability of III–V Nanowire Arrays. *Applied Physics Reviews* **2021**, *8* (1), 011304. https://doi.org/10.1063/5.0031549.
(5) Castaing, R. & Slodzian, G. J. Optique Corpusculaire—Premiers Essais de Microanalyse Par Emission Ionique Secondaire. *J Microscopie 1* **1962**, 395–399.
(6) Kelly, T. F.; Miller, M. K. Atom Probe Tomography. *Rev. Sci. Instrum.* **2007**, *78* (031101), 21. https://doi.org/10.1063/1.2709758.
(7) Anderson, D. A.; Apsley, N. The Hall Effect in III-V Semiconductor Assessment. *Semicond. Sci. Technol.* **1986**, *1* (3), 187–202. https://doi.org/10.1088/0268-1242/1/3/006.
(8) Chawla, B. R.; Gummel, H. K. Transition Region Capacitance of Diffused P-n Junctions. *IEEE Trans. Electron Devices* **1971**, *18* (3), 178–195. https://doi.org/10.1109/T-ED.1971.17172.
(9) Lucia, M. L.; Hernandez-Rojas, J. L.; Leon, C.; Mártil, I. Capacitance Measurements of P-n Junctions: Depletion Layer and Diffusion Capacitance Contributions. *Eur. J. Phys.* **1993**, *14* (2), 86–89. https://doi.org/10.1088/0143-0807/14/2/009.
(10) Lassiaz, T.; Tchoulfian, P.; Donatini, F.; Brochet, J.; Parize, R.; Jacopin, G.; Pernot, J. Nanoscale Dopant Profiling of Individual Semiconductor Wires by Capacitance–Voltage Measurement. *Nano Lett.* **2021**, *21* (8), 3372–3378. https://doi.org/10.1021/acs.nanolett.0c04491.
(11) Rau, W. D.; Schwander, P.; Baumann, F. H.; Höppner, W.; Ourmazd, A. Two-Dimensional Mapping of the Electrostatic Potential in Transistors by Electron Holography. *Physical Review Letters* **1999**, *82* (12), 2614–2617. https://doi.org/10.1103/PhysRevLett.82.2614.
(12) den Hertog, M.; Songmuang, R.; Monroy, E. Polarization Fields in GaN/AlN Nanowire Heterostructures Studied by off-Axis Holography. *J. Phys.: Conf. Ser.* **2013**, *471*, 012019. https://doi.org/10.1088/1742-6596/471/1/012019.

(13) Twitchett, A. C.; Dunin-Borkowski, R. E.; Midgley, P. A. Quantitative Electron Holography of Biased Semiconductor Devices. *Phys. Rev. Lett.* **2002**, *88* (23), 238302. https://doi.org/10.1103/PhysRevLett.88.238302.
(14) Cooper, D.; Ailliot, C.; Truche, R.; Barnes, J.-P.; Hartmann, J.-M.; Bertin, F. Experimental Off-Axis Electron Holography of Focused Ion Beam-Prepared Si p-n Junctions with Different Dopant Concentrations. *Journal of Applied Physics* **2008**, *104* (6), 064513. https://doi.org/10.1063/1.2982415.
(15) Gan, Z.; Perea, D. E.; Yoo, J.; Tom Picraux, S.; Smith, D. J.; McCartney, M. R. Mapping Electrostatic Profiles across Axial *p-n* Junctions in Si Nanowires Using off-Axis Electron Holography. *Appl. Phys. Lett.* **2013**, *103* (15), 153108. https://doi.org/10.1063/1.4824775.
(16) Anada, S.; Yamamoto, K.; Sasaki, H.; Shibata, N.; Hori, Y.; Kinugawa, K.; Imamura, A.; Hirayama, T. Precise Measurement of Electric Potential, Field, and Charge Density Profiles across a Biased GaAs p-n Tunnel Junction by in Situ Phase-Shifting Electron Holography. *J. Appl. Phys.* **2017**, *122* (22), 225702. https://doi.org/10.1063/1.5006837.
(17) den Hertog, M.; Donatini, F.; McLeod, R.; Monroy, E.; Sartel, C.; Sallet, V.; Pernot, J. *In Situ* Biasing and off-Axis Electron Holography of a ZnO Nanowire. *Nanotechnology* **2018**, *29* (2), 025710. https://doi.org/10.1088/1361-6528/aa923c.
(18) He, K.; Cho, J.-H.; Jung, Y.; Tom Picraux, S.; Cumings, J. Silicon Nanowires: Electron Holography Studies of Doped p–n Junctions and Biased Schottky Barriers. *Nanotechnology* **2013**, *24* (11), 115703. https://doi.org/10.1088/0957-4484/24/11/115703.
(19) Conlan, A. P.; Moldovan, G.; Bruas, L.; Monroy, E.; Cooper, D. Electron Beam Induced Current Microscopy of Silicon *p–n* Junctions in a Scanning Transmission Electron Microscope. *Journal of Applied Physics* **2021**, *129* (13), 135701. https://doi.org/10.1063/5.0040243.
(20) Zhou, R.; Yu, M.; Tweddle, D.; Hamer, P.; Chen, D.; Hallam, B.; Ciesla, A.; Altermatt, P. P.; Wilshaw, P. R.; Bonilla, R. S. Understanding and Optimizing EBIC P-n Junction Characterization from Modeling Insights. *Journal of Applied Physics* **2020**, *127* (2), 024502. https://doi.org/10.1063/1.5139894.
(21) Shibata, N.; Findlay, S. D.; Sasaki, H.; Matsumoto, T.; Sawada, H.; Kohno, Y.; Otomo, S.; Minato, R.; Ikuhara, Y. Imaging of Built-in Electric Field at a p-n Junction by Scanning Transmission Electron Microscopy. *Sci Rep* **2015**, *5* (1), 10040. https://doi.org/10.1038/srep10040.
(22) Haas, B.; Rouvière, J.-L.; Boureau, V.; Berthier, R.; Cooper, D. Direct Comparison of Off-Axis Holography and Differential Phase Contrast for the Mapping of Electric Fields in Semiconductors by Transmission Electron Microscopy. *Ultramicroscopy* **2019**, *198*, 58–72. https://doi.org/10.1016/j.ultramic.2018.12.003.
(23) Clark, L.; Brown, H. G.; Paganin, D. M.; Morgan, M. J.; Matsumoto, T.; Shibata, N.; Petersen, T. C.; Findlay, S. D. Probing the Limits of the Rigid-Intensity-Shift Model in Differential-Phase-Contrast Scanning Transmission Electron Microscopy. *Phys. Rev. A* **2018**, *97* (4), 043843. https://doi.org/10.1103/PhysRevA.97.043843.
(24) Müller, K.; Krause, F. F.; Béché, A.; Schowalter, M.; Galioit, V.; Löffler, S.; Verbeeck, J.; Zweck, J.; Schattschneider, P.; Rosenauer, A. Atomic Electric Fields Revealed by a Quantum Mechanical Approach to Electron Picodiffraction. *Nat Commun* **2014**, *5* (1), 5653. https://doi.org/10.1038/ncomms6653.
(25) Müller-Caspary, K.; Grieb, T.; Müßener, J.; Gauquelin, N.; Hille, P.; Schörmann, J.; Verbeeck, J.; Van Aert, S.; Eickhoff, M.; Rosenauer, A. Electrical Polarization in AlN/GaN Nanodisks Measured by Momentum-Resolved 4D Scanning Transmission Electron Microscopy. *Phys. Rev. Lett.* **2019**, *122* (10), 106102. https://doi.org/10.1103/PhysRevLett.122.106102.
(26) Beyer, A.; Munde, M. S.; Firoozabadi, S.; Heimes, D.; Grieb, T.; Rosenauer, A.; Müller-Caspary, K.; Volz, K. Quantitative Characterization of Nanometer-Scale Electric Fields via Momentum-Resolved STEM. *Nano Lett.* **2021**, *21* (5), 2018–2025. https://doi.org/10.1021/acs.nanolett.0c04544.
(27) da Silva, B. C.; Momtaz, Z. S.; Bruas, L.; Rouviere, J.-L.; Okuno, H.; Cooper, D.; den-Hertog, M. I. The Influence of Illumination Conditions in the Measurement of Built-in Electric Field at p–n Junctions by 4D-STEM. *Applied Physics Letters* **2022**, *121* (12), 123503. https://doi.org/DOI: 10.1063/5.0104861.
(28) Cooper, D. Off-Axis Electron Holography for the Measurement of Active Dopants in Silicon Semiconductor Devices. *J. Phys. D: Appl. Phys.* **2016**, *49* (47), 474001. https://doi.org/10.1088/0022-3727/49/47/474001.
(29) Delille, D.; Pantel, R.; Van Cappellen, E. Crystal Thickness and Extinction Distance Determination Using Energy Filtered CBED Pattern Intensity Measurement and Dynamical Diffraction Theory Fitting. *Ultramicroscopy* **2001**, *87* (1–2), 5–18. https://doi.org/10.1016/S0304-3991(00)00067-X.
(30) Hyperspy. https://hyperspy.org (Accessed: 20 March 2022).
(31) Bruas, L.; Boureau, V.; Conlan, A. P.; Martinie, S.; Rouviere, J.-L.; Cooper, D. Improved Measurement of Electric Fields by Nanobeam Precession Electron Diffraction. *Journal of Applied Physics* **2020**, *127* (20), 205703. https://doi.org/10.1063/5.0006969.

(32) Xiao, C.; Yang, D.; Yu, X.; Xiang, L.; Que, D. Determination of the Boron and Phosphorus Ionization Energies in Compensated Silicon by Temperature-Dependent Luminescence. *Silicon* **2017**, *9* (2), 147–151. https://doi.org/10.1007/s12633-014-9193-3.
(33) Tchoulfian, P.; Donatini, F.; Levy, F.; Dussaigne, A.; Ferret, P.; Pernot, J. Direct Imaging of p–n Junction in Core–Shell GaN Wires. *Nano Lett.* **2014**, *14* (6), 3491–3498. https://doi.org/10.1021/nl5010493.
(34) Cooper, D.; Twitchett-Harrison, A. C.; Midgley, P. A.; Dunin-Borkowski, R. E. The Influence of Electron Irradiation on Electron Holography of Focused Ion Beam Milled GaAs P-n Junctions. *Journal of Applied Physics* **2007**, *101* (9), 094508. https://doi.org/10.1063/1.2730557.

TABLES

Table 1 – Theoretical calculations of the maximum electric field, depletion region width and built-in potential for a silicon *p-n* junction with different doping levels, considering the abrupt and linearly graded approximations. The equations derived for both approximations can be found in the Supplementary Information (SI5). The experimental results have been added for comparison.

	E_{max} $(MV cm^{-1})$	W_d (nm)	V_{bi} (V)
Experimental (4D-STEM)	0.176 ± 0.03	73 ± 11	0.88 ± 0.06
Experimental (Electron Holography)	0.175 ± 0.02	--	0.86 ± 0.05
Abrupt p-n junction $(N_A = N_D = 9.0 \times 10^{18} cm^{-3})$	0.859	12	1.06
Abrupt p-n junction $(N_A = N_D = 4.5 \times 10^{17} cm^{-3})$	0.178	51	0.906
Abrupt p-n junction $(N_A = N_D = 2.8 \times 10^{17} cm^{-3})$	0.138	64	0.881
Linearly graded p-n junction $(\alpha = 1.5 \times 10^{23} cm^{-4})$	0.176	78	0.918

FIGURE CAPTIONS

Figure 1 – Schematic of the momentum-resolved 4D-STEM experiment performed in a silicon *p-n* junction. Reverse bias is obtained by applying a negative bias ($-V_{bias}$) to the *p*-side, while the *n*-side is grounded.

Figure 2 – (a) In-situ biased 4D-STEM electric field maps of the silicon *p-n* junction. (b) Profiles of the electric field obtained from the maps shown in (a) by integration along the entire map, as indicated in (a). The measured depletion length for zero bias is indicated, following the method used by[16] extrapolating an almost linear region of the electric field profile symmetrically around the full-width at half-maximum value of the field strength.

Figure 3 – (a) In-situ biased 4D-STEM charge density maps of the silicon *p-n* junction. (b) Profiles of the charge density obtained from (a) by integration along the entire map, as indicated in (a).

Figure 4 – Comparison between the values of maximum electric field measured by in-situ biased 4D-STEM and the expected evolution with bias considering a linearly graded *p-n* junction with various impurity gradients, α.

Figure 5 – (a) Dopant profile (blue), $N_D - N_A$, with an intermediate graded region extending over 200 nm consisting of a linearly graded *p-n* junction with an impurity gradient of $\alpha = 1.5 \times 10^{23} cm^{-4}$. Outside the intermediate region, the dopant concentration is the bulk value $N_A = N_D = 9 \times 10^{18} cm^{-3}$. (b) and (c) Comparison between simulated and experimental electric field and charge density at zero bias, respectively. In (b) and (c), we demonstrate that an impurity gradient of $\alpha = 1.8 \times 10^{23} cm^{-4}$ (magenta) provides a better fit due to the partial compensation of thermal effects.

FIGURE 1

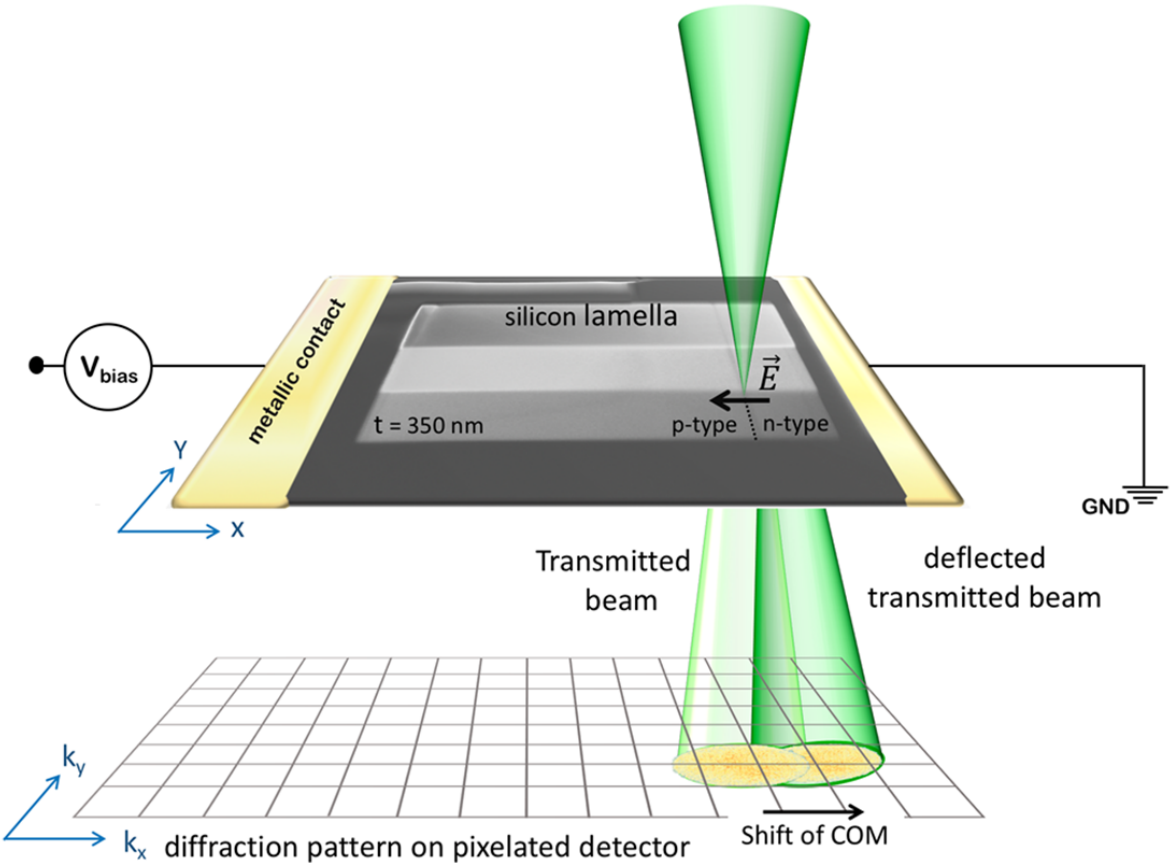
silicon lamella
metallic contact
V_{bias}
$\vec{E}$
t = 350 nm
p-type
n-type
GND
Y
X
Transmitted beam
deflected transmitted beam
k_y
k_x
diffraction pattern on pixelated detector
Shift of COM

FIGURE 2

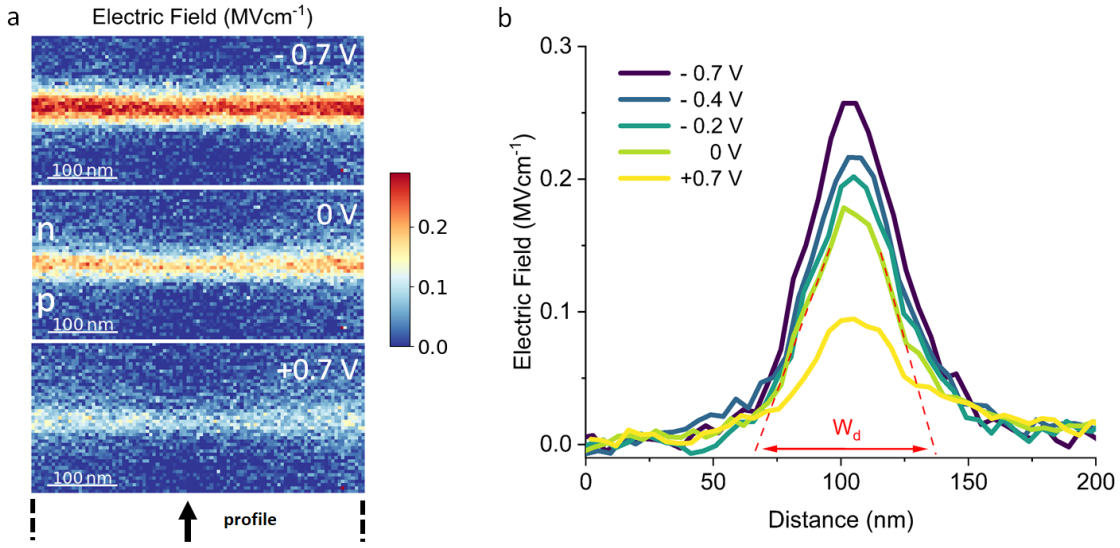
a
Electric Field (MVcm-1)
- 0.7 V
100 nm
n
0 V
p
100 nm
+0.7 V
100 nm
profile
0.2
0.1
0.0
b
0.3
0.2
0.1
0.0
Electric Field (MVcm-1)
- 0.7 V
- 0.4 V
- 0.2 V
0 V
+0.7 V
Wd
0
50
100
150
200
Distance (nm)

FIGURE 3

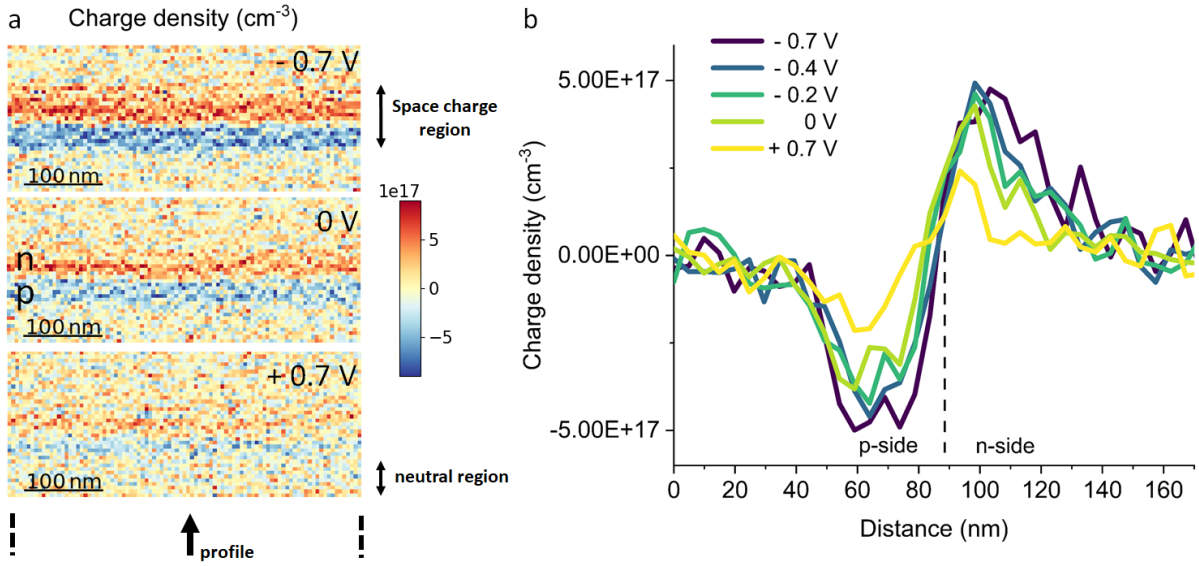
a
Charge density (cm-3)
- 0.7 V
100 nm
0 V
n
p
100 nm
+ 0.7 V
100 nm
Space charge region
1e17
5
0
−5
neutral region
profile
b
- 0.7 V
- 0.4 V
- 0.2 V
0 V
+ 0.7 V
5.00E+17
0.00E+00
-5.00E+17
Charge density (cm-3)
p-side
n-side
0
20
40
60
80
100
120
140
160
Distance (nm)

FIGURE 4

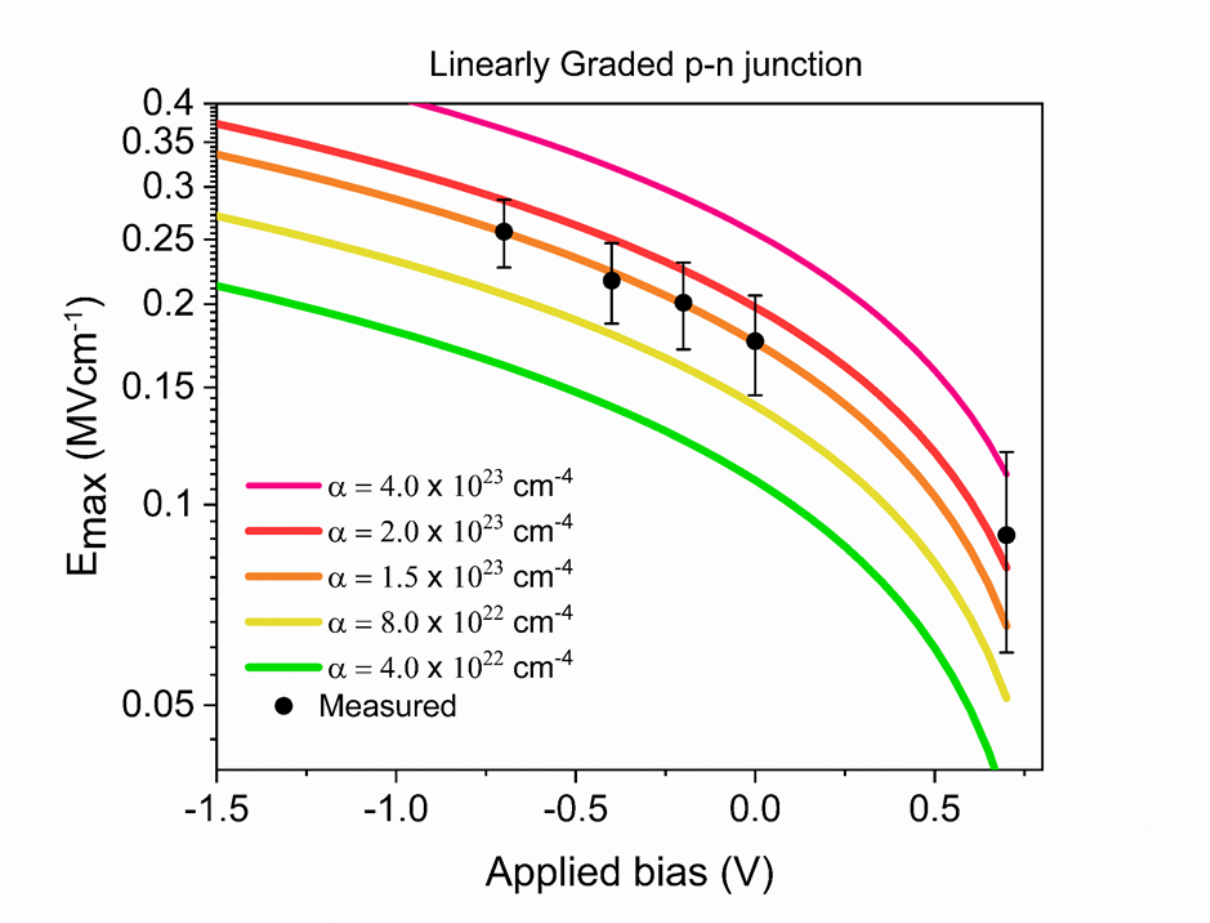
Linearly Graded p-n junction
Emax (MVcm-1)
0.4
0.35
0.3
0.25
0.2
0.15
0.1
0.05
-1.5
-1.0
-0.5
0.0
0.5
Applied bias (V)
α = 4.0 x 10^23 cm^-4
α = 2.0 x 10^23 cm^-4
α = 1.5 x 10^23 cm^-4
α = 8.0 x 10^22 cm^-4
α = 4.0 x 10^22 cm^-4
Measured

FIGURE 5

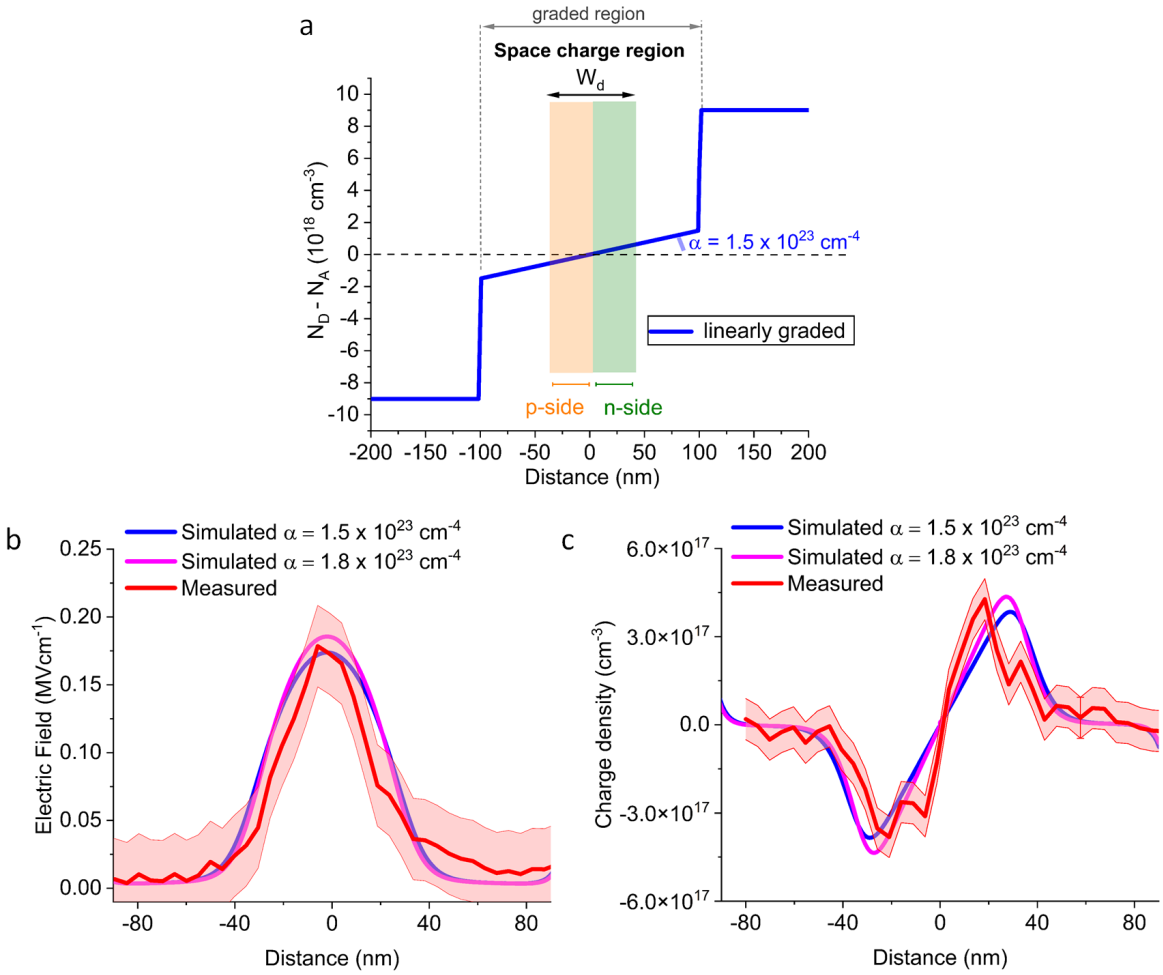
a
graded region
Space charge region
W_d
$N_D - N_A$ (10^{18} cm^{-3})
α = 1.5 x 10^{23} cm^{-4}
linearly graded
p-side
n-side
Distance (nm)
b
Simulated α = 1.5 x 10^{23} cm^{-4}
Simulated α = 1.8 x 10^{23} cm^{-4}
Measured
Electric Field (MVcm^{-1})
Distance (nm)
c
Simulated α = 1.5 x 10^{23} cm^{-4}
Simulated α = 1.8 x 10^{23} cm^{-4}
Measured
Charge density (cm^{-3})
Distance (nm)

TOC Figure

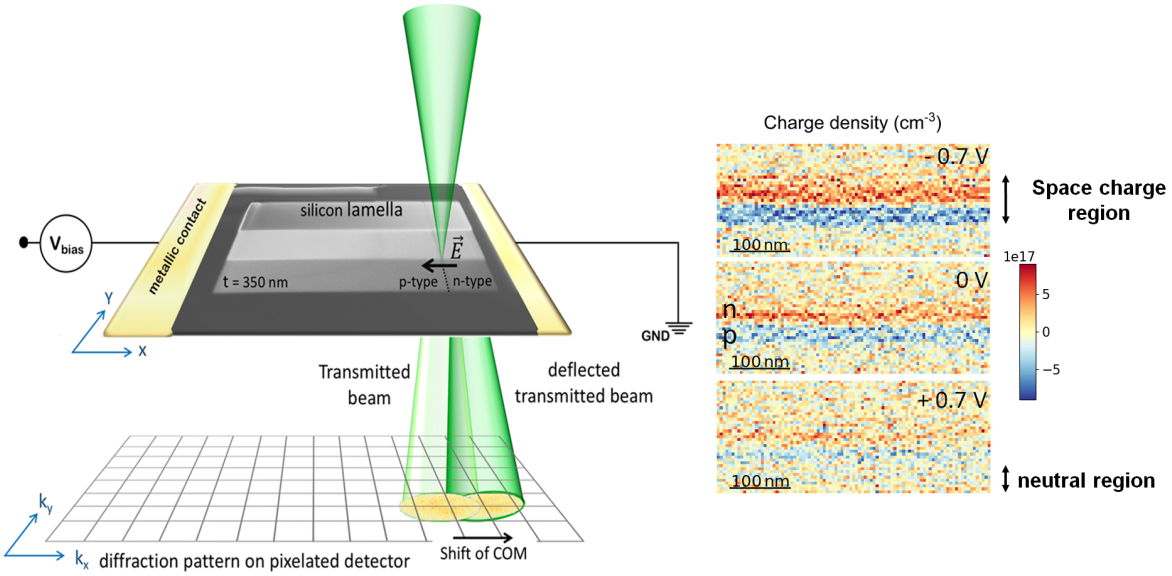
Charge density (cm-3)
- 0.7 V
Space charge region
100 nm
1e17
5
0
−5
0 V
n
p
100 nm
+ 0.7 V
100 nm
neutral region
silicon lamella
metallic contact
t = 350 nm
p-type
n-type
Vbias
GND
Y
X
Transmitted beam
deflected transmitted beam
ky
kx
diffraction pattern on pixelated detector
Shift of COM